Journal of Alloys and Compounds 1037 (2025) 182111

Contents lists available at ScienceDirect

Journal of Alloys and Compounds

journal homepage: www.elsevier.com/locate/jalcom

Post hot-deformation precipitation behavior of γ′ phase in VDM® alloy 780 under varying cooling rates and aging temperatures: An in situ high energy XRD study

M. Fritton [a,*], O. Nagel [b], F. Kümmel [a], A. Stark [c], M. Hafez-Haghighat [d], B. Gehrmann [d], S. Neumeier [b], R. Gilles [a]

[a] Technische Universität München, MLZ, Lichtenbergstr. 1, Garching 85748, Germany
[b] Friedrich-Alexander-Universität Erlangen-Nürnberg, Martensstr. 5, Erlangen 91058, Germany
[c] Helmholtz-Zentrum hereon GmbH, Max-Planck-Straße 1, Geesthacht 21502, Germany
[d] VDM Metals International GmbH, Zeilweg 42, Frankfurt am Main 65439, Germany

ARTICLE INFO

Keywords:
Ni-based superalloys
γ′ precipitation
High-energy X-ray diffraction (HE-XRD)
Cooling rate effects
Age-hardening
In situ XRD
Phase fraction evolution

ABSTRACT

The performance of polycrystalline Ni-based superalloys is largely determined by the fraction and size of the intermetallic hardening phases, such as the γ′ phase. Understanding the evolution of the γ′ precipitate size and volume fraction during the complex thermomechanical process chain is essential for optimizing the mechanical properties of polycrystalline Ni-based superalloys. In this study, the high temporal resolution of in situ synchrotron X-ray diffraction at elevated temperatures was used to monitor γ′ evolution in VDM® Alloy 780 during cooling and subsequent aging heat treatments in real time. To simulate the industrial forging process, the alloy was initially subjected to compressive deformation at 1000 °C. In the first part of the study, immediately after hot forming, three different cooling rates (10 °C/min, 100 °C/min, and 1000 °C/min) were applied to analyse the in situ evolution of γ′ precipitation. The resulting γ′ phase fraction was highest at the slowest cooling rate, yet even the fastest cooling rate did not completely suppress precipitation. In the second part of the study, the age-hardening response of the alloy was examined at holding temperatures of 720 °C and 800 °C for five hours each. The evolution of the γ′ volume fraction, precipitate size, and lattice parameter was monitored in situ by XRD. After aging, γ′ volume fractions of 15 % and 19 % were obtained, with average precipitate sizes of 9 nm and 18 nm, respectively. The prior deformation enhanced γ′ formation at 720 °C compared to literature data. Complementary Transmission Electron Microscopy (TEM) measurements confirmed precipitate sizes consistent with the diffraction data.

1. Introduction

Higher operating temperatures in both jet engines and stationary gas turbines are required to increase their efficiency, i.e., to reduce CO_2 emissions and fulfill the European Green Deal. Polycrystalline Ni-based superalloys are inevitable for such challenging applications where the material is subjected to a combination of high thermal and mechanical loads in corrosive environments [1–3]. The workhorse of polycrystalline Ni-based superalloys is Alloy 718, commonly known as Inconel; however, its application temperature is limited to 650 °C [4,5].

To increase the possible application temperatures and yield higher efficiencies, the VDM® Alloy 780 (DIN no. 2.4960) was developed for applications at temperatures of up to 750 °C under high mechanical load [6,7]. In comparison to Alloy 718, most of the Fe and a fraction of Ni have been replaced by Co while the Al content has been increased and the Ti content reduced in VDM® Alloy 780 [8]. These chemical modifications lead to the exclusive formation of the γ′ phase with a limited solvus temperature and hinder the formation of the γ″ phase, which is the major hardening phase in Alloy 718 [9]. The γ″ phase is stable up to approximately 650 °C, above which significant coarsening and its transformation into the δ-phase sets in, which limits its application temperature. Since the γ″ phase does not form in the VDM® Alloy 780, this restriction does not exist.

In the fully aged condition, this superalloy consists of nanoscale

* Corresponding author.
E-mail address: Massimo.Fritton@frm2.tum.de (M. Fritton).

https://doi.org/10.1016/j.jallcom.2025.182111
Received 27 March 2025; Received in revised form 23 May 2025; Accepted 5 July 2025
Available online 8 July 2025

intermetallic γ′ precipitates (Ni_3Al-based, $L1_2$) coherently embedded in the γ matrix (Ni-based, A1) and micron-sized high-temperature stable phases (HT-phases) δ and η (δ, Ni_3Nb-based, D0a; η, Ni_3Ti-based, $D0_{24}$) [8,10–12]. The high-temperature phases impede grain growth during forging by pinning the grain boundaries [9]. Minor amounts of carbides (NbC, A1), well below 1 vol%, form during the alloy's solidification process [13]. The high mechanical strength of more than 1500 MPA at RT the alloy is largely attributed to the comparably large γ′ volume fraction (approximately 35 %) and the coherent embedding of the γ′ precipitates (< 50 nm) in the γ matrix [14–16]. The VDM® Alloy 780 features a significant positive lattice misfit of approximately 0.38 % at room temperature, which gradually decreases with increasing temperature due to the slightly higher thermal expansion coefficient of the γ phase[9]. However, the lattice misfit remains around 0.34 % at 750 °C, which is important for the performance at elevated temperatures [13]. At temperatures above 800 °C, the γ′ phase begins to dissolve. This leads to a reduction in lattice misfit, as Al and Nb—both elements with larger atomic radii—dissolve into the γ matrix, causing an increase in its lattice parameter, consistent with Vegard's law. This dependency, i.e., the influence of the γ′ volume fraction on the lattice parameter of the matrix, was also observed by Solis et al., who found that the γ matrix lattice parameters were smallest at the highest γ′ volume fraction and vice versa.

[10] The largest γ matrix lattice parameters occur when no γ′ has formed, and consequently, all elements with larger atomic radii are dissolved. With increasing the amount of γ′, the matrix gets depleted in these bigger atoms, and thereby the lattice parameter decreases [13].

Bergner et al. investigated the effect of heat treatment procedure on the microstructure evolution and mechanical properties of a slightly modified version of VDM® Alloy 780 by a combination of SEM and Vickers hardness testing. They observed a sluggish precipitation of the HT phase at 850 °C, while significant precipitation occurred at higher temperatures of 900 °C - 975 °C in the as-forged condition [17]. Additionally, the precipitation of γ′ was investigated at 800 °C and 650 °C, following HT-phase precipitation at 900 °C and a γ′ solution heat treatment at 955 °C.

A particularly strong effect of the cooling rate from 955 °C to 800 °C was observed, which significantly influenced the microstructure evolution and mechanical properties of the alloy. Air cooling and furnace cooling were compared, with air cooling leading to higher strength due to finer γ′ precipitates [17]. This is reflected in higher HV10 hardness values for air-cooled samples (474 for air-cooled and 420 for furnace-cooled) and significantly longer stress rupture times at 700 °C [17].

Sajjadi et al. investigated the effect of different cooling rates on the γ′ volume fraction and precipitate size in Udimet 500, and found that increasing cooling rates resulted in a lower γ′ volume fraction and smaller precipitates [18].

This demonstrates the strong influence of the cooling rate on the microstructure and the mechanical properties of superalloys which, however, has not yet been systematically studied for VDM® Alloy 780. Therefore, in this study, three different cooling rates from an initial super-solvus temperature of 1000 °C were applied, and their influence on γ′ -phase precipitation was investigated in situ using high-energy X-ray diffraction (HE-XRD). The high temporal resolution of the synchrotron enables real-time monitoring of precipitation during cooling. Studying different cooling rates is important since cooling rates during the manufacturing process of the same component can vary greatly depending on the respective position.

The strengthening mechanism of precipitate-hardened alloys follows a common principle. At high temperatures, above the solvus temperature of the precipitates, all alloying elements remain dissolved within the matrix. In the case of ageing, the initial supersaturation within the matrix is predetermined by the prior temperature treatment. As the isothermal process progresses, the formation and growth of γ′ precipitates gradually reduce supersaturation[19]. In contrast, during continuous cooling precipitation, the evolution of supersaturation is influenced by a complex interplay of competing mechanisms. On one hand, supersaturation builds up continuously due to ongoing cooling, while on the other hand, it is simultaneously consumed by the nucleation and growth of γ′ precipitates. The extent to which these opposing processes affect supersaturation depends strongly on the cooling rate. At lower cooling rates, less undercooling occurs, leading to a lower degree of supersaturation within the matrix [19].

Before cooling, the alloy was compressively deformed at 1000 °C. During hot deformation, subgrain formation and grain rotation into preferred orientations led to significant microstructural changes, which were investigated in detail in our recent publication [9].

In the next step of this study—after hot deformation and cooling—the precipitation heat treatment was studied at temperatures of 720 °C and 800 °C for five hours each. This is an important step ahead, as previous studies were performed without prior deformation. The process more closely resembles industrial conditions, where forging, simulated here by hot deformation, is carried out before aging. In an initial study by Solis et al., the aging was investigated at 720 °C and 620 °C without prior deformation [20]. Using a combination of small-angle neutron scattering (SANS) and time of flight neutron diffraction (TOF ND) they in situ monitored the precipitation and growth of γ′ in VDM® Alloy 780 [20]. Their observations showed pronounced nucleation and precipitate growth for the fully solutionized sample (WB0) at 720 °C, while during the second stage of the heat treatment at 620 °C, precipitate size remained stable, and the volume fraction increased slightly [20].

On the one hand, the aging temperature of 720 °C in this study was selected, to isolate the influence of the hot deformation by comparing the results with those of Solis et al. [20] On the other hand, the aging temperature of 800 °C was chosen, to assess how the higher diffusion rates at elevated temperatures affect γ′ precipitation behavior. Diffusion behavior of the γ′-forming elements Al and Nb in Ni was evaluated in a previous study by fitting the time-dependent penetration depth using an Arrhenius-type relation. The reported values represent effective diffusion coefficients derived from a $\sqrt{t}$-type growth law, expressed as linear rate constants with units of $nm/s^{-1/2}$. At 720 °C, rate constants of 2.98 $nm/s^{-1/2}$ for Nb and 3.07 $nm/s^{-1/2}$ for Al were determined, while at 800 °C, they increased to 11.47 $nm/s^{-1/2}$ for Nb and 12.89 $nm/s^{-1/2}$ for Al, respectively [13]. This corresponds to an approximately fourfold increase in the effective diffusion kinetics with a temperature rise of 80 °C.

To examine the kinetics of precipitation during aging, the well-established Johnson-Mehl-Avrami-Kolmogorov (JMAK) model can be utilized [21]. This model characterizes isothermal phase transformations through the following relationship:

$$\frac{f(t)}{f_{eq}} = \frac{(c_0 - c(t))}{(c_0 - c_\alpha)} = 1 - \exp(-k(T)\ t^n) \quad (1)$$

In this context, $f(t)$ represents the time-dependent volume fraction of the transformed phase, corresponding to the precipitates. The parameters c_0 and c_α denote the initial solute concentration and the equilibrium concentration at a given temperature, respectively, while $c(t)$ represents the solute concentration in the matrix at time t. Since the volume fraction of precipitates f_t is directly linked to the depletion of solute, it asymptotically approaches an equilibrium value f_{eq} as the solute concentration reaches c_α. $k(T)$ is a kinetic parameter that depends on the actual aging temperature as well as the nucleation and growth rates, and it is typically described using an Arrhenius-type relationship. Meanwhile, the parameter n is Avrami's exponent, which indicates the rate of nucleation and/or the nature of the growth morphology. When the equilibrium volume fraction is reached—meaning precipitation is complete—continued aging can lead to coarsening of the precipitates. This spontaneous, thermodynamically driven process, known as Ostwald ripening, occurs because larger precipitates, being energetically favored, grow at the expense of smaller ones [22,23].

For the industrial production of polycrystalline Ni-based superalloys, the precipitation of the hardening phase is a crucial process, as it directly defines the material's mechanical properties. Therefore, it is of utmost importance to study the formation of γ′ both during cooling and aging using HE-XRD. A major advantage of in situ studies over conventional methods, which only examine the microstructure after heat treatment at room temperature, is that they capture the dynamic evolution of the microstructure during the process. In contrast, many widely applied techniques such as electron microscopy only provide the final outcome without revealing the transformation pathway.

2. Experimental

Table 1 shows the chemical composition of the main elements of VDM® Alloy 780. The alloy, provided in rod form with a diameter of 17 mm, was heat treated at 1080 °C for 1 h, followed by water quenching (WQ). The fully recrystallized microstructure exhibited an average grain size of approximately 70 μm without preferred grain orientation, as shown in a recent publication [9]. All experiments presented in this study used material from the same batch. The parameters of the performed cooling and aging experiments are shown in Fig. 1.

The samples used for the XRD measurements were cylindrical, with 10 mm in length and 5 mm in diameter; they were machined from the rod using a lathe and subsequently separated using a cut-off machine. XRD experiments were performed at the High Energy Material Science (HEMS) beamline at PETRA III, DESY (Hamburg, Germany), using a short wavelength of 0.124 Å, enabling deep penetration into the highly absorbing alloy. The X-ray beam spot size on the sample was approximately 1 mm^2, leading to an illuminated volume of roughly 6 mm^3 , as the sample diameter increased by approximately 1 mm due to compression; considering the total sample volume of about 200 mm^3 , this corresponds to roughly 3 % of the entire specimen being probed.

The compression was performed using a dilatometer (DIL 805 A/D, TA Instruments, Hüllhorst, Germany) [24], which is equipped with a hydraulic compression device that measures the distance between two Si_3N_4 stamps with a displacement transducer. To mimic the industrial forging process, the alloy was compressed at a deformation rate of 1×10^{-3} s^{-1} to approximately a 20 % height reduction at 1000 °C. Although higher deformation rates are used in industry, the conditions chosen here still resemble the industrial process. The material was heated at a rate of 1000 °C/min to minimize microstructural changes during heating. In addition, available synchrotron beamtime could be used more efficient. The temperature of 1000 °C was chosen to ensure deformation in the γ single-phase region, preventing premature precipitation of γ′. This was confirmed by the absence of γ′ superstructure reflections in the diffractogram, indicating that, if at all, only tiny amounts of less than 1 vol% could be present[9]. Directly after hot deformation, the specimens were cooled to 500 °C using three different cooling rates (10 °C/min, 100 °C/min, and 1000 °C/min) by controlled Ar gas blowing. Below 500 °C, the samples were cooled to 50 °C at the maximum possible cooling rate to save valuable experiment time, since no microstructural changes occur below this temperature. In the final step, the samples were aged for five hours at either 720 °C or 800 °C and then cooled to 50 °C again at the maximum cooling rate. Diffractograms were continuously recorded throughout the heating and deformation processes described above.

Full Debye-Scherrer rings were recorded using a flat panel detector (XRD1621, Perkin Elmer, Norwalk, CT, USA) positioned at a distance of 1600 mm from the sample. Diffraction patterns were acquired at a rate of up to 5 Hz to ensure a sufficient number of measuring points despite the partially very high temperature ramps of up to 1000 °C/min. The image detector has a resolution of 2048 × 2048 pixels, each measuring 200 × 200 μm, and the primary beam hit the detector center, which was covered by a beamstop. The samples were heated using an induction coil, and the temperature was tracked *via* a spot-welded S-type thermocouple. To enable analysis *via* Rietveld refinements, the 2D raw data were treated using the Fit2D software [25]. Rietveld refinements were performed to determine volume fractions, lattice parameters, and average precipitate sizes using the FullProf software [26].

To determine the γ′ volume fraction during continuous cooling (Fig. 3), the γ′-(100) superlattice reflection was individually fitted at each time step. The integrated peak areas were then normalized to the value obtained at 500 °C, where a full Rietveld refinement was performed to calibrate the absolute volume fraction. This reference value served as a scaling factor to estimate the γ′ volume fractions at higher temperatures. The approach enabled a time-efficient evaluation of phase evolution while maintaining quantitative consistency.

The profiles were fitted using the Thompson-Cox-Hastings approximation. The zero shift, lattice parameters, size and strain parameters, atomic positions, and thermal displacement parameters were refined, while the background was corrected using a series of adjustable points. The average γ′ precipitate size was calculated using FullProf based on the Scherrer equation, as the full-width at half-maximum (FWHM) is influenced by the size when the precipitates are significantly smaller than 100 nm [27]. The instrumental parameters were determined through a calibration measurement using standardized lanthanum hexaboride (LaB_6), which is known to exhibit neither size nor strain effects. This calibration enabled the determination of the Cagliotti parameters (U, V, W) by performing a complete refinement of the LaB_6 standard, thereby isolating the peak broadening caused by the instrument. The remaining peak broadening of the γ′ phase was fitted by refining the Gaussian (IG) and Lorentzian (Y) contributions of the reflection profile. This approach allowed estimation of the average precipitate sizes of the γ′ phase.

The microstructural analysis was performed using a *Philips CM200* transmission electron microscope (TEM) operated at 200 kV, to determine whether and in what average size γ′ has formed. Image analysis was performed using the ImageJ software package (National Institutes of Health, USA). TEM samples were prepared by cutting discs approximately 400 μm thick, perpendicular to the load axis, from the inner regions of the specimens. These were ground to a thickness of about 100 μm and subsequently electropolished in a *Struers Double Jet Tenupol-5* at 25 °C and 50 V using a solution of 16.7 % nitric acid and 83.3 % methanol. To investigate the influence of different cooling and aging heat treatments on the mechanical properties of VDM® Alloy 780, Vickers hardness HV10 measurements were performed using a hardness testing machine from *Schütz+Licht*. For each sample, five measurements were taken, and the average value was determined.

Thermodynamic calculations were performed using the Thermo-Calc software version 2023b, with the TCNI12 database (version 12.1) for Ni-based Alloys. For these calculations, the nominal chemical composition was used (cf. Table 1). Based on the composition, the equilibrium volume fractions of γ and γ′ at 720 °C and 800 °C were calculated.

Table 1
Nominal chemical composition of VDM® Alloy 780 without consideration of minor elements such as B or C.

	Ni	Co	Cr	Fe	Mo	Nb	Al	Ti
wt%	Balance	24.4	17.7	0.6	2.9	5.4	2.2	0.3

3. Results and discussion

3.1. Precipitation at different cooling rates

Except for the carbides, all phases can be dissolved in the γ matrix. The HT phases exhibit sluggish precipitation kinetics in VDM® Alloy 780 and have a solvus temperature of approximately 1020 °C while the solvus temperature of the γ′ phase is approximately 970 °C [13]. To investigate the precipitation of the HT-phases, longer exposure times are required, which is beyond the scope of this study. Bergner et al. studied the precipitation of the HT-phase *via* SEM at temperatures ranging from 850 °C to 975 °C in 25-degree increments for up to 16 h [17].

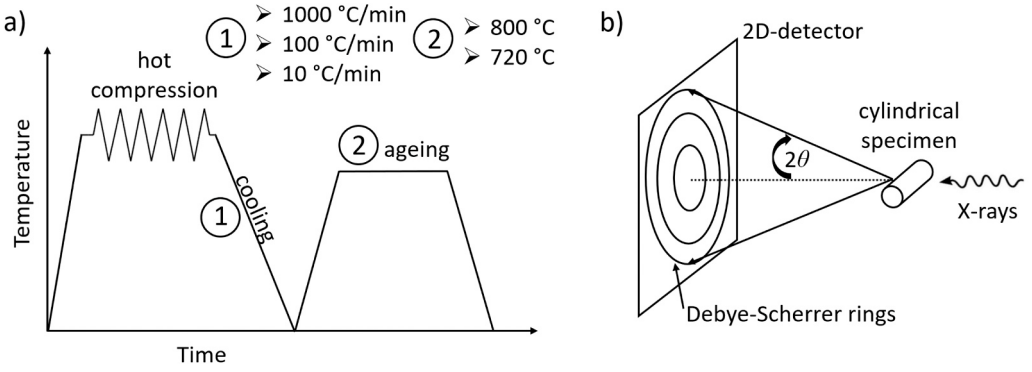

Fig. 1. a) Scheme of the performed cooling and aging experiments after deformation at 1000 °C and b) experimental setup for the diffraction experiments.

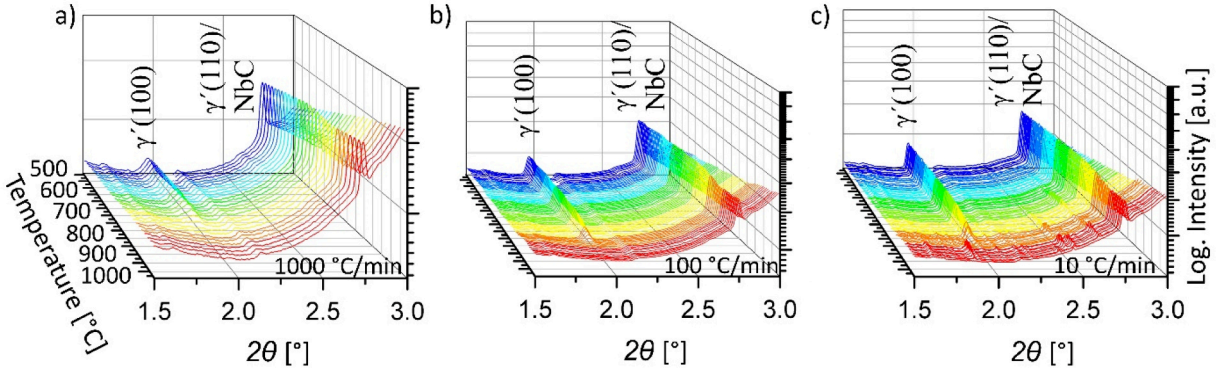

Fig. 2. In situ XRD pattern measured from 1000 °C to 500 °C, during cooling with a) 1000 °C/min, b) 100 °C/min and, c) 10 °C/min. The selected 2θ range covers the isolated γ′-(100) reflection, as well as the combined γ′-(110)/NbC (111) reflection.

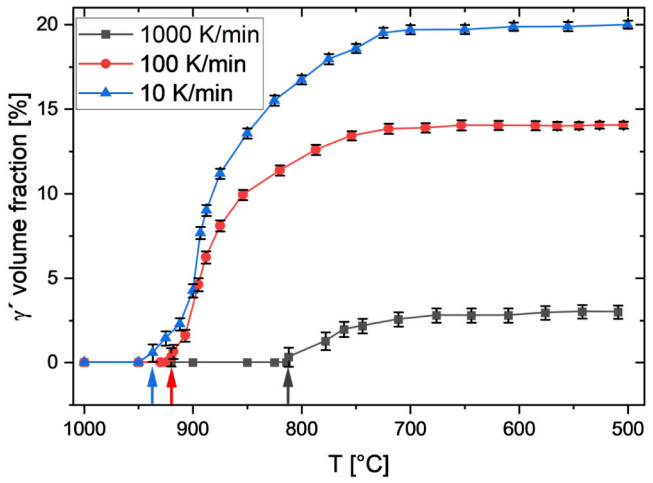

Fig. 3. Evolution of the γ′ volume fraction for different cooling rates between 1000 °C and 500 °C, determined by single peak fitting of the γ′-(100) reflection. The solid lines serve as visual guides to illustrate the trend. Arrows in the respective colors indicate the onset temperatures of γ′ precipitation.

3.1.1. In situ synchrotron diffraction

In the following, precipitation in fully solutionized VDM® Alloy 780 samples is studied exclusively after compressive deformation at 1000 °C. This temperature is slightly above the γ′ solvus temperature, ensuring that forging is mimicked in the single-phase domain. During forging dynamic recrystallisation was observed in our previous study [9]. Directly after hot deformation, the precipitation of γ′ was investigated under different cooling rates of 10 °C/min, 100 °C/min, and 1000 °C/min. Thereby, a wide range of cooling rates is covered which is important as in industrial manufacturing the cooling rates after forging can also vary significantly. In general, cooling rates are higher at the edges than in the inner part and decrease with increasing mass and decreasing surface-to-volume ratio. The thermal conductivity is also important, as a high thermal conductivity decreases temperature gradients in a workpiece. It is worth noting that the highest cooling rate of 1000 °C/min is still significantly slower than water quenching, where several hundred °C/s can be reached [28]. The slow cooling rate of 10/°C min corresponds to typical furnace cooling rates. The intermediate cooling rate of 100 °C/min was selected to have a step between the fast and slow cooling rate.

From the Rietveld refinements (cf. Fig. 4), the influence of different cooling rates on the final microstructures can be observed. However, the microstructural evolution during cooling remains elusive. A simple and illustrative way to visualize the in situ data on γ′ precipitation is to stack the diffractograms in order of decreasing temperature. This is presented in Fig. 2, where only the low 2 θ range from (1.5° to 3°) is displayed, as precipitation is most evident in this region.

Due to the high cooling rate in Fig. 2a and the acquisition time for each 2D diffraction pattern, a smaller number of diffractograms was recorded compared to the lower cooling rates in Fig. 2b and c. In contrast, for the slowest cooling rate, only every 10th diffractogram is displayed in Fig. 2c. Fig. 2c also exhibits some small additional peaks, that may result from slight surface oxidation effects due to the slow cooling process and associated prolonged exposure to high temperatures. The onset temperatures for γ′ precipitation were determined as 811 °C, 918 °C, and 937 °C for cooling rates of 1000 °C/min, 100 °C/min, and 10 °C/min, respectively. This aligns with the expected trend that higher cooling rates lead to more pronounced undercooling.

To determine the onset temperatures, the isolated γ′-(100) reflection was used. However, onset temperatures can also be determined using

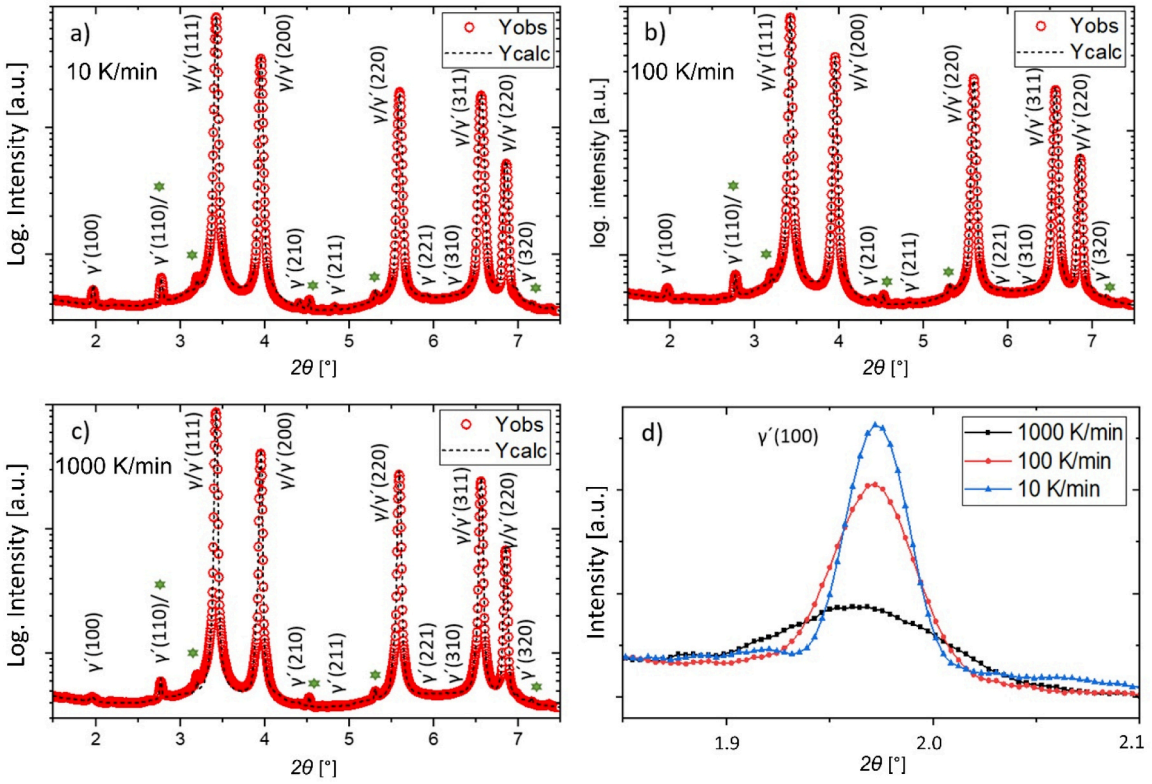

Fig. 4. Rietveld refinement of the VDM® Alloy 780 samples measured at room temperature after hot forming and cooling to RT with a) 10 °C/min, b) 100 °C/min, and c) 1000 °C/min. The observed data are shown by red circles, the calculated data by a dotted black line, the Bragg reflections of NbC by green stars, and the Bragg reflections are marked by γ and γ′. The γ′-(100)-reflection of the three experiments is shown magnified in d).

the combined γ′-(110)/NbC reflection, as the NbC content remains constant over the tested temperature range. Thus, an increase in the intensity of this reflection corresponds to γ′ precipitation. By applying a regression line and interpolation to 0 °C/min, a solvus temperature of 935 °C was obtained (cf. SI, Figure S1). In our recent study conducted on the same instrument, a solvus temperature between 950 °C and 970 °C was determined *via* incremental heating, during which the γ′-(100) superstructure reflection completely disappeared [13]. The slight difference between the measured temperatures for complete dissolution and initial nucleation may be attributed to the need for supercooling during precipitation and slight overheating for dissolution. That is, the precipitation temperature is always lower than the dissolution temperature. Below 600 °C, no further increase in the γ′-phase fraction was observed for any of the three cooling rates tested. The FWHM of the reflections decreases with decreasing cooling rate, which can be explained by the increasing average precipitate sizes. To quantitatively describe precipitation, Fig. 3 illustrates the evolution of the γ′ volume fraction during cooling.

At 1000 °C, all γ′-forming elements (Al, Nb, Ti) are fully dissolved in the matrix. As the temperature decreases, the solubility of these elements reduces, promoting precipitation. The onset temperatures of precipitation, as stated above, are also visible in Fig. 3, which shows significant undercooling for the fastest cooling rate. The curves for the three cooling rates exhibit a sigmoidal shape, which is characteristic of precipitation processes [29]. Such a sigmoidal trend can be divided into three main stages: nucleation, precipitate growth, and coarsening.

In the initial phase, the precipitation rate is low because nanosized nuclei must form first. Once a sufficient number of nuclei has developed, the volume fraction increases more rapidly—this corresponds to the steepest part of the curve, where existing precipitates grow significantly. In the final phase, the system approaches saturation since the temperatures becomes too low and the solutes become immobile, leading to a gradual decline in precipitation rate until a steady state is reached.

For the medium and slow cooling rates, the overall evolution follows a similar trend, with slightly shifted precipitation onset temperatures. The most pronounced increase in precipitate volume fraction occurs around 900 °C. By 850 °C, precipitation has already slowed significantly and continues at a reduced rate until approximately 700 °C, below which no further increase in volume fraction is observed. The γ′ volume fractions at 500°C are approximately 20 % for the slow cooling rate and 14 % for the medium cooling rate. During cooling, thermodynamic equilibrium may be approached at distinct temperatures, inhibiting a further increase in volume fraction at this temperature, or the temperature may drop below a threshold where precipitation is suppressed.

In an infinitely slow cooling process, where thermodynamic equilibrium is maintained at all temperatures, the γ′ volume fraction would continuously adjust according to equilibrium conditions. For slow cooling rates, precipitation approaches closer to thermodynamic equilibrium. However, as the cooling rate increases, the system deviates further from equilibrium, and kinetic effects such as undercooling become more dominant. This trend is particularly evident for the fastest cooling rate, where the resulting microstructure is far from thermodynamic equilibrium due to the strong influence of kinetics.

Rapid cooling at 1000 °C/min results in strong undercooling, which significantly impacts the evolution of the microstructure. Once nuclei have formed, the growth kinetics are already slowed due to the lower temperature and the associated reduction in diffusion rates. Additionally, the limited time spent at each temperature step further restricts the increase in volume fraction. The γ′ growth period, roughly between 800 °C and 675 °C, lasts only approximately 8 s at 1000 °C/min. This resulted in only about 3 vol% of the hardening phase being formed at 675 °C; below this temperature no further increase in volume fraction was observed. Below 500 °C, the specimens were cooled to RT at the maximum possible rate, as no further changes in the microstructure are expected. Fig. 4 presents RT Rietveld refinements after applying the three distinct cooling rates.

Since the main γ and γ′ reflections overlap significantly, the superstructure reflections of γ′ (γ′-(100) & -(110) at low angles) are crucial for data evaluation. The (110) reflection, however, overlaps with NbC. Therefore, the (100) reflection was used to determine the profile parameters. Tiny amounts of NbC are always present but remain unaffected by the aging and cooling experiments performed here. For the lowest cooling rate, the γ′-volume fraction is 20 %, and for the medium cooling rate, 14 % after cooling to RT. Even rapid cooling at 1000 °C/min cannot completely suppress precipitation and leads to a γ′ volume fraction of 3 %. These values are consistent with those observed at 500 °C (cf. Fig. 3) and show that below 500 °C no further γ′ precipitation is observed.

Average γ′ precipitate size values of 43 nm, 21 nm, and 8 nm were obtained after cooling to RT for cooling rates of 10 °C/min, 100 °C/min, and 1000 °C/min, respectively. Strictly speaking, this corresponds to the average size of coherent scattering regions, which will be treated synonymously with precipitate size in the following. Complementary TEM measurements were performed on identically treated samples (cf. Fig. 5) to verify these trends. The (100) superstructure reflections in Fig. 4c additionally shift to lower 2θ angles with decreasing cooling rate, indicating a decreasing lattice parameter but increasing average precipitate sizes and volume fractions. γ′-phase lattice parameters of 3.616 (6) Å, 3.6157(2) Å, 3.60175(1) Å were obtained by Rietveld refinements after cooling at 1000 °C/min, 100 °C/min, and 10 °C/min, respectively. Due to the combination of a low γ′ volume fraction and broad, irregularly shaped peaks, the error in the lattice parameter is more than an order of magnitude larger for the high cooling rate. This correlation between the γ′ phase fraction and its lattice parameter has also been observed in previous studies of VDM® Alloy 780 [10,20]. The reason is that the lower the γ′ volume fraction, the higher the fraction of γ′-forming elements with larger atomic radii (such as Al, Ti, and Nb) in the γ matrix phase. As the γ′ phase fraction increases, fewer large γ′-formers are available, leading to a smaller lattice parameter.

3.1.2. Microstructure after cooling

To support the HE-XRD results, the samples were also examined using TEM measurements. Since the influence of the cooling rate on the matrix phase was already investigated in a previous study [9], only high-magnification images are shown to enable the identification of the hardening phase precipitates.

Fig. 5 shows TEM images after applying the different cooling rates. A decrease in precipitate sizes with increasing cooling rates is observed. This behavior is expected and can be explained by the prolonged time at the respective temperatures during which precipitate growth occurs. From the images in Fig. 5, average precipitate sizes were determined using image analysis. Precipitate sizes of 57 nm, 21 nm, and 6 nm were obtained from the TEM images with decreasing cooling rate. Table 2 summarizes the TEM-derived precipitate size values in comparison with XRD-derived values. The precipitates in Fig. 5a fall within the range of 60 nm, which is larger than the diffraction-derived average of 43 nm. The increased distance between precipitates indicates advanced Ostwald ripening. At the medium cooling rate, precipitates are much smaller (~20 nm), which is almost identical to the XRD value of 21 nm. At the highest cooling rate, γ′ precipitates are visible only at higher magnification (cf. Fig. 5c), with average sizes of approximately 6 nm, which agree well with diffraction-based values. The TEM measurements confirm that the evaluation of precipitate sizes using diffraction is a valid approach.

Table 2
Volume fraction and average precipitate size obtained by XRD and TEM.

Cooling rate [°C/min]	γ′ Volume fraction [%]	γ′ Precipitate size [nm]	
	XRD	XRD	TEM
10	20.2 ± 0.6	43.3 ± 0.1	57.2 ± 7.4
100	14.0 ± 0.7	21.2 ± 0.1	20.6 ± 4.6
1000	2.9 ± 0.1	8.1 ± 0.0	5.8 ± 1.8

3.1.3. Vickers hardness

The mechanical properties, such as hardness are strongly influenced by the volume fraction and size of the γ′ precipitates. Generally, hardness increases with an increasing amount of γ′ [30,31]; however, grain size, precipitate size, texture, and dislocation density also influence hardness [32]. To gain insight into the correlation between γ′ and the mechanical properties of the alloy, additional HV tests were performed on the specimens. Table 3 lists the HV values for the three different cooling rates as well as for the γ′-free, undeformed fully solutionized reference.

The significantly higher HV values after hot deformation and subsequent cooling at the three cooling rates, compared to the fully solutionized reference indicate the presence of the hardening phase and an increased dislocation density due to the compression deformation. From EBSD measurements conducted as part of our previous study, recrystallized fractions of 63 %, 25 %, and 35 % were determined with increasing cooling rates, relative to the fully recrystallized reference [9]. Deformed grains exhibit more dislocations than recrystallized grains

Table 3
HV10 of the VDM® Alloy 780 samples depending on the cooling rate after forging.

Cooling rate [°C/min]	HV10
10	408.3 (8.7)
100	413.1 (7.9)
1000	334.7 (6.2)
Reference (fully solutionized)	259.1 (4.1)

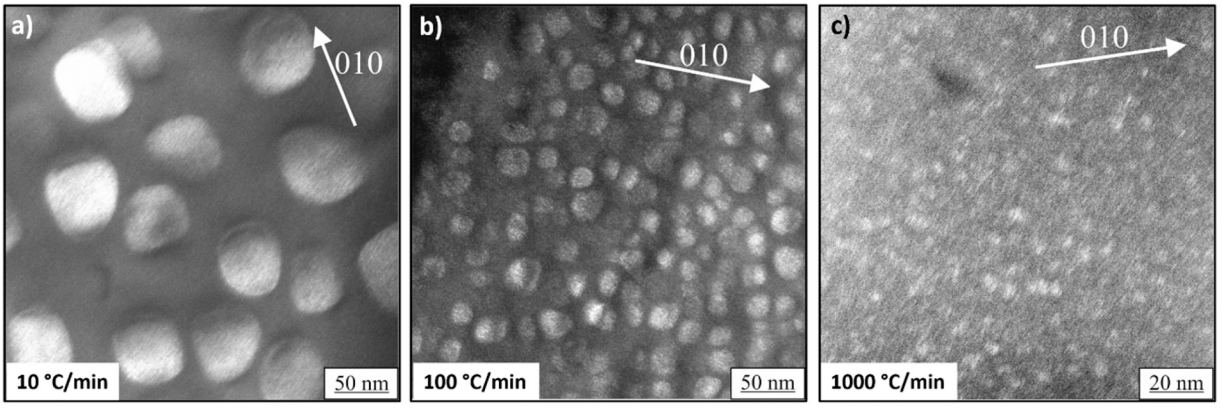

Fig. 5. TEM dark field images of the VDM® Alloy 780 after hot deformation at 1000 °C and cooling to RT with a) 10 °C/min, b) 100 °C/min, and c) 1000 °C using g = (010) in two-beam conditions.

which increases the material's hardness [33,34]. Therefore, the difference in hardness values—259 HV10 for the reference sample and 334 HV10 for the fast-cooled sample—can be attributed to both the higher dislocation density and the small amount of γ′ precipitates in the fast-cooled condition. Additionally, the smaller grain size, i.e., the increased grain boundary area, enhances hardness, as grain boundaries act as barrier to dislocation movement [35,36]. This is also known as the Hall-Petch relationship [37,38]. The hardening phase precipitates, which are coherently embedded in the matrix, further increase the alloy's strength as a/2 < 110 > {111} dislocations traveling through γ cannot enter the γ′ phase without forming planar defects, such as an anti-phase boundary (APB), which incurs a high energy penalty. The fast and medium cooling rates result in hardness values of 334 HV10 and 413 HV10, respectively. These conditions exhibit similar recrystallized fractions and grain sizes, but different γ′ phase fractions, leading to higher hardness for the medium cooling rate. Interestingly, the medium cooling rate results in slightly higher hardness compared to the slow cooling condition, despite the lower γ′ phase fraction. A reasonable explanation is that the average γ′ precipitate size is significantly smaller at the medium cooling rate, which can enhance hardness despite a lower volume fraction. The smaller precipitates are more closely spaced, which increases the frequency of dislocation–precipitate interactions and promotes dislocation multiplication [39]. In contrast, the larger and more widely spaced precipitates formed during slow cooling are less effective in impeding dislocation motion, which may explain the reduced hardness observed in this condition. Additionally, the lower cooling rate enables a greater extent of recrystallization, reducing dislocation density and consequently material hardness. A decrease in hardness with increasing precipitate size was also reported by Ali et al. for single crystal superalloys [30]. Their study further demonstrates that, when the precipitate size is held constant, hardness increases with increasing the γ′ volume fraction [30]. A similar trend—higher HV10 values at a lower γ′ phase fraction but smaller precipitates—was observed by Solis et al. for VDM® Alloy 780 samples with slightly different microstructures [10]. In the following, the effects of the aging heat treatment on the microstructure and mechanical properties are examined.

3.2. Precipitation during aging

Directly after hot forming at 1000 °C and cooling to RT at 1000 °C/min, the aging behavior at 800 °C and 720 °C was investigated. The high cooling rate of 1000 °C/min was selected to minimize premature γ′ precipitation, with only a tiny amount of precipitates (approximately 3 vol%) being formed (cf. Fig. 4c). The nucleation and growth of γ′ precipitates are mechanisms that may occur simultaneously during aging, making the process complex [40]. The age-hardening step is comparatively studied for approximately 5 h at both temperatures.

3.2.1. In situ synchrotron diffraction

The influence of the different aging temperatures on the microstructure is presented in the following. It is illustrative to stack the diffractograms of the in situ measurements to show the evolution of precipitation at the respective temperatures. Fig. 6 shows the evolution of the γ′ precipitates by stacking the isolated (100) reflections with increasing aging time.

Since almost 5000 patterns were recorded in each of the 5-hour measurements, only every 30th pattern was used for the graphical representation in Fig. 6. This corresponds to approximately one diffractogram every two minutes. At both temperatures, the intensity of the γ′-(100) reflection increases, which can be due to the nucleation of new crystallites or the growth of already existing ones. At 800 °C, the most significant changes are observed at the very beginning, where the intensity increases strongly and the FWHM decreases, which is associated with an increase in both the overall volume fraction and the average precipitate size. After these abrupt changes at the beginning, only slower changes in peak intensity and shape are observed. At 720 °C the intensity also increases right at the beginning while the FWHM changes are only moderate indicating increasing volume fraction but limited average precipitate growth. At 720 °C, the γ′-(100) reflection features small average precipitate sizes, i.e., a large FWHM value, even after 5 h of aging. To quantify the assumptions made here, selected patterns were evaluated by individual Rietveld refinements. At both temperatures, the VDM® Alloy 780 specimens were aged for approximately 5 h and diffraction patterns were continuously acquired to investigate the precipitation and growth of γ′ with time. Fig. 7a shows the evolution of the γ′ volume fraction and average precipitate size and Fig. 7b the evolution of the hardening phase lattice parameter with time at temperatures of 800 °C and 720 °C.

In Figs. 7a and 7b the first data point was collected as soon as the temperature had stabilized at the respective temperature and is set to zero, as acquiring one diffraction image takes about 3 s. The number of patterns evaluated was minimized to enable the visualization of parameter (volume fraction, average size) evolution over time as all patterns were evaluated by individual Rietveld refinements. Since major changes in the microstructure occur right at the beginning of the aging treatment for both temperatures, primarily due to the rapid increase in γ′ volume fraction, data with smaller time steps were evaluated in this region. During the first hour, approximately one data point was analyzed every 8 min, while at later stages, only about two points per hour were selected. During aging both, the precipitate size and the volume fraction of the hardening phase are affected by nucleation and nuclei growth which can occur simultaneously. The initial γ′ volume fraction, i.e., the volume fraction at 0 ks is higher at 800 °C than at 720 °C. A possible explanation for this is that for both experiments, the samples were heated to their respective temperatures at the same heating rate, which results in longer heating for the 800 °C sample. During heating between 720 °C and 800 °C, precipitation can occur, leading to the observed difference. We do not observe a sigmoidal-

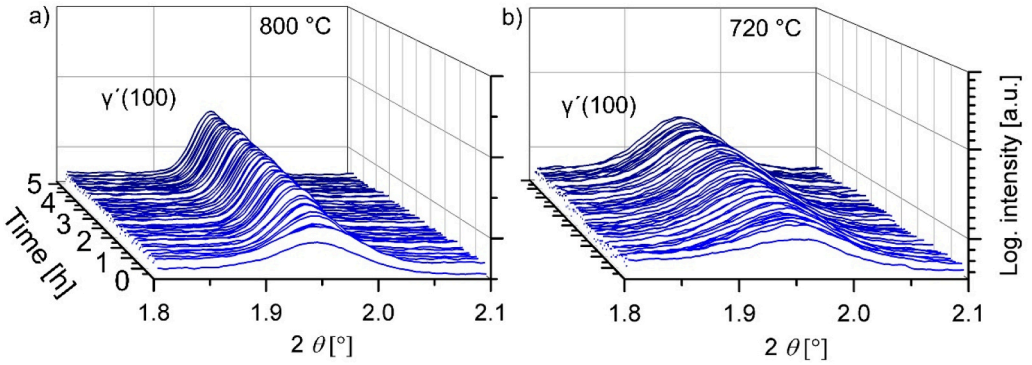

Fig. 6. In situ XRD diffractograms acquired for 5 h at a) 800 °C and b) 720 °C, respectively. The selected 2 θ range covers the isolated γ′-(100) reflection.

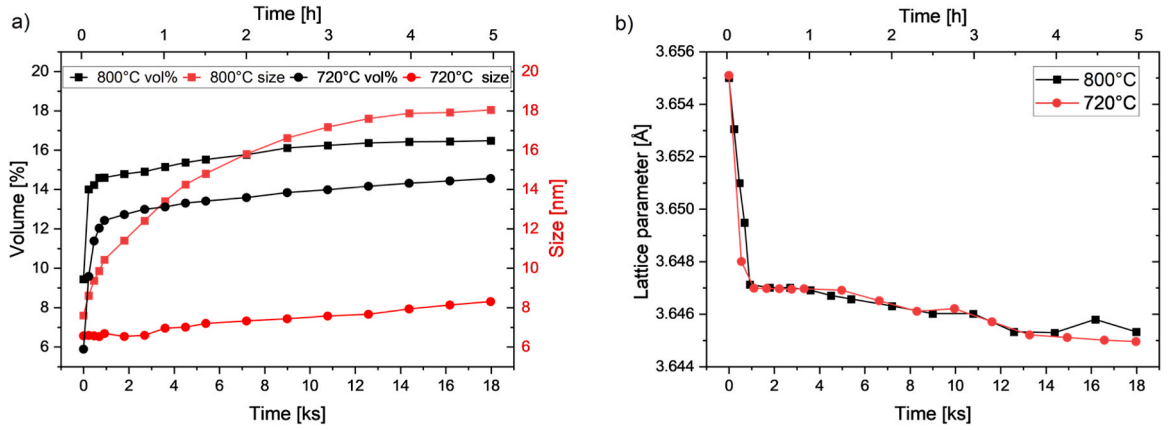

Fig. 7. Evolution of the γ′ volume fraction and size with time (a) and evolution of the γ′ lattice parameter for the aging temperatures of 800 °C and 720 °C. The squares correspond to the temperature of 800 °C and the spheres to 720 °C. The line between the data serves only as a guide for the eye.

shaped curve as in Fig. 3, since the initial phase—nucleation—is already well advanced. Therefore, the strong volume fraction increase in the first minutes, at both temperatures corresponds to the growth of precipitates. This is followed by a slow linear increase after approximately half an hour at 720 °C and approximately 15 min at 800 °C. At 720 °C, the linear increase continues until the end of the aging treatment, resulting in a volume fraction of 14.5 %. This suggests that precipitation at this temperature is not yet complete, i.e., the equilibrium state has not yet been reached. At 800 °C, the linear behavior continues up to approximately 9 ks (2.5 h), after which the total volume fraction gain is only minor. A possible explanation could be that the equilibrium volume fraction of slightly more than 16 % at 800 °C is almost reached after 2.5 h. This assumption is corroborated by calculations performed using the Thermo-Calc software, see chapter 3.2.3. with Table 3.

The evolution of the average precipitate size differs significantly between the two tested temperatures. Initially, similar average sizes of around 6–7 nm and 7–8 nm are found for 720 °C and 800 °C, respectively but at the lower temperature, a moderate linear increase is observed, while at the higher temperature, the precipitates exhibit strong initial growth, which subsequently slows down. Ultimately, aging at 800 °C results in an average precipitate size of about 18 nm, whereas at 720 °C, the average size remains significantly smaller, at approximately 8 nm. The moderate increase in average size at 720 °C could be due to slower diffusion rates and the correspondingly lower precipitate growth rate.

At 800 °C, a volume fraction of more than 14 % is reached with an average precipitate size of less than 9 nm after approximately 5 min, from which point the volume fraction increases only slightly, but the average precipitate size continues to grow. The increasing size may be due to precipitate growth, where the γ′-forming elements are consumed from the matrix, or due to Ostwald ripening, where larger precipitates grow at the expense of smaller ones. However, Ostwald ripening usually occurs at a constant volume fraction, i.e., when precipitation is complete, leading to fewer but larger precipitates. This could explain the behavior between 5 ks and 14 ks at 800 °C, where the volume fraction increases only slightly, but the average size still increases significantly. With coarsening, the average distance between precipitates increases, explaining how this process mitigates itself. It should be noted that after 5 h of aging at 800 °C, a tiny amount of HT phase has formed but remains significantly below 1 vol%. This is evident from weak reflections between the main γ-(111) and γ-(200) reflections (cf. SI, Figure S4). At 720 °C, no HT-phase reflections were observed after aging.

From the evolution of the volume fraction during aging, Eq. 1 was used to fit the data (SI Figure S5) and thereby obtain values for the Avrami parameter (n) and the kinetic parameter (k). Avrami parameters n of 0.33 and 0.17 were derived for 720 °C and 800 °C, respectively. These values are relatively low; however, in the study by Solis et al., a similar Avrami parameter of 0.23 was obtained by in situ SANS measurements at 720 °C for the same alloy and heat treatment[20]. Such small values have been reported in literature for superalloys and steels and have been associated with the nucleation of intermetallic phases along dislocations[20,41]. The higher Avrami parameter of 0.33 compared to the 0.23 determined by Solis et al. at 720 °C might be due to the higher dislocation density as a direct consequence of the hot deformation at the beginning of our experiments. The k values were determined to be 0.15 at 720 °C and 0.72 at 800 °C. Here, the value at 720 °C is smaller than that in the study by Solis et al. but still falls within a comparable range[20]. At 800 °C, the value is significantly higher. This can be explained by the fact that higher temperatures lead to enhanced diffusion processes, which accelerate growth. As a result, the overall transformation velocity increases, as reflected by the higher k value.

When looking at the evolution of the γ′ lattice parameter (cf. Fig. 7b), a rapid decrease is observed in the beginning, followed by a slower linear reduction after approximately 30 min for both aging temperatures. As mentioned above, the initial precipitates contain a higher concentration of γ′-forming elements with larger atomic radii. With increasing γ′ volume fraction, the lattice parameter decreases due to the dilution of these elements. For both temperatures, the first lattice parameter value is approximately 3.655 Å, from which it continues to decrease due to ongoing γ′ precipitation. Therefore, the rapid initial decrease is attributed to the strong increase in γ′ volume fraction for both temperatures. Subsequently, the lattice parameter decreases linearly, corresponding to the linear increase in volume fraction during this period. Interestingly, both lattice parameter curves are very similar, despite the larger γ′ phase fraction at 800 °C. This suggests that the compositional evolution of the precipitates during aging follows a comparable trend at both temperatures. At 800 °C, the lattice parameter remains stable after 12 ks, which is consistent with the constant volume fraction during this period. In contrast, at 720 °C, the γ′ lattice parameters continue to decrease until the end of the experiment, in accordance with ongoing precipitation. This trend—i.e., the correlation between γ′ volume fraction and lattice parameter—has also been observed in previous studies[20].

Fig. 8 shows the Rietveld refinements after the entire thermo-mechanical treatment, which includes compressive deformation at 1000 °C, cooling to RT at 1000 °C/min, aging at 800 °C and 720 °C, respectively, and subsequent cooling to RT. After aging, cooling was performed at the maximum possible rate to minimize changes in the microstructure for further microscopic investigations.

The RT Rietveld refinements provide γ′ volume fractions of 19 % and 15 %, and average precipitate sizes of 19 nm and 9 nm after aging at 800

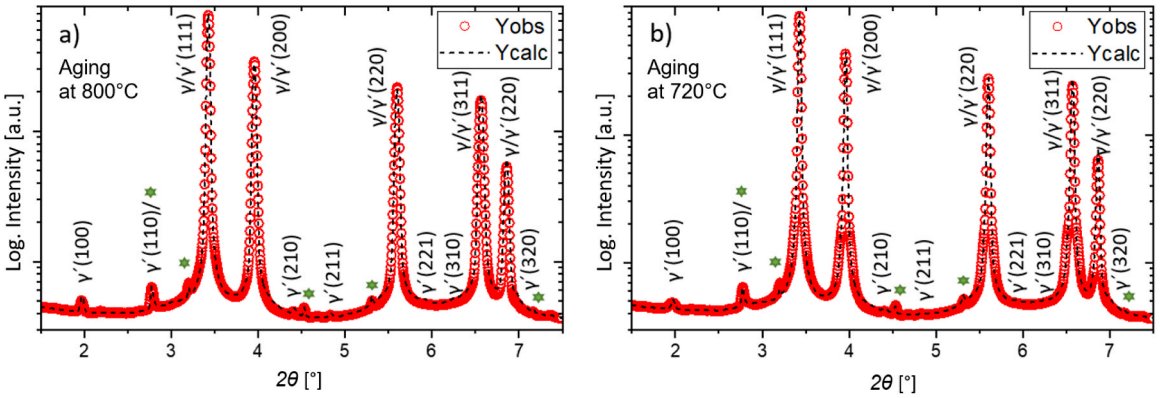

Fig. 8. Rietveld refinement of the VDM® Alloy 780 samples tested at room temperature after hot forming and cooling to RT 1000 °C/min and 5 h aging at a) 800 °C, and b) 720 °C. The observed data are shown by red circles, the calculated data by a dotted black line, the Bragg reflections of NC by green stars, and the Bragg reflections are marked by γ and γ′.

°C and 720 °C for 5 h, respectively. These values are in close agreement with the values at the end of the aging heat treatment for both temperatures. This demonstrates that quenching at the end of the aging heat treatment hinders further significant changes in the microstructure, i.e., freezes the condition. Both the average size and the volume fraction of the hardening phase increase by applying the aging temperature of 800 °C for 5 h. The average size and volume fraction values at 720 °C are close to the TOF ND (average size approximately 10 nm, volume fraction approximately 10 %) and SANS (size approximately 5 nm, volume fraction approximately 12 %) values determined by Solis et al. after 5 h aging at 720 °C [20]. The volume fraction of 15 % is increased compared to the TOF ND and SANS values. The hot deformation at the beginning of the experiments likely contributes to the observed differences, as it generates dislocations and grain boundaries, which are well-known to act as heterogeneous nucleation sites and facilitate diffusion[5,42]. This suggests that while hot deformation prior to aging does not fundamentally alter the precipitation behavior during aging, but it affects the volume fraction of the hardening phase, which is of importance for the final application.

3.2.2. *Microstructure after aging*

After the entire thermomechanical treatment, i.e., compressive deformation at 1000 °C, fast cooling to RT, and five hours of aging at 800 °C and 720 °C, TEM images were acquired at RT.

The TEM images in Figs. 9a and 9b show the γ′ precipitates. After aging at 800 °C, the precipitates are significantly larger compared to aging at 720 °C. From these images, average precipitate sizes were determined to be 23 nm and 11 nm for 800 °C and 720 °C, respectively, in good agreement with the size calculation *via* diffraction. A bigger distance between the precipitates is recognized at 800 °C, indicating Ostwald ripening. Thereby the images support the assumption that the coarsening process was already completed at 800°C (cf. Fig. 7). At this point, it is important to mention that the determination of volume fractions and average sizes by microscopy can be subject to significant errors due to the limited statistics in the small areas measured. For determining volume fractions via TEM measurements, additionally, the foil thickness needs to be known, which was not the case in our study. If the samples are inhomogeneous the errors can be even greater. Overall, the microscopy and diffraction values agree well, confirming the validity of the combination of diffraction and imaging techniques.

3.2.3. *Thermodynamic calculations*

Additionally, Thermocalc (TC) simulations were performed for the two aging temperatures, and the values are also shown in Table 3. However, the values determined with TC apply to thermodynamic equilibrium, i.e., after an infinitely long time.

At 800 °C, the TC-derived values are in close agreement with the TEM (cf. Fig. 9) and XRD (cf. Fig. 8) values. The in situ XRD

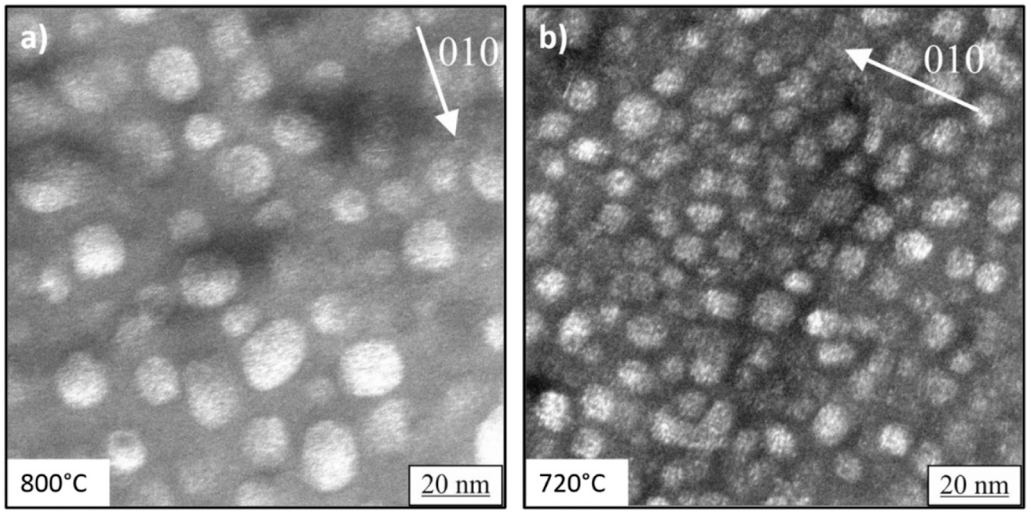

Fig. 9. TEM dark field images images of the VDM® Alloy 780 after hot deformation at 1000 °C cooling to RT with 1000 °C/min, aging at a) 800 °C and b) 720 °C, and cooling to RT using g = (010) in two-beam conditions.

measurements at 800 °C showed a constant volume fraction after about 2.5 h (cf.Fig. 7), which indicates that the equilibrium volume fraction was reached at this temperature. This explains the good agreement, as in both cases, i.e., in the experiment and in the simulation, the thermodynamic equilibrium is reached.

At 720 °C, the TC-derived value of 23.7 is significantly higher than the diffraction-derived value of 14 vol%. However, when observing the progression of the γ′ volume fraction at 720 °C in Fig. 7, it becomes evident that the equilibrium state has not yet been reached, i.e., the volume fraction is still increasing. Therefore, the TC-predicted volume fractions, which assume thermodynamic equilibrium, cannot be directly compared with the values after approximately 5 h at 720 °C, where precipitation is not yet completed. Table summarizes the precipitate size and volume fraction values obtained by the two complementary techniques XRD and TEM and the TC simulations.

3.2.4. Vickers hardness

Vickers hardness measurements have been carried out after aging heat treatments and cooling to RT. HV10 values of 446 and 405 were obtained after aging with 800 °C and 720 °C, respectively. This difference of approximately 10 % may be explained by the higher γ′ volume fraction after aging at 800 °C, as it is known that higher volume fractions of precipitates enhances hardness [31]. Although the precipitate size is larger after aging at 800 °C, it remains within the range where dislocations can still shear the γ′ precipitates.

After slow cooling, the precipitate volume fraction of 20 % was slightly higher than the 19 % observed after aging at 800 °C. Nevertheless, the hardness is significantly higher for the aged specimen. This difference can be attributed to the precipitate size and spacing: the smaller γ′ precipitates formed during aging are more closely spaced, which enhances dislocation–precipitate interactions and promotes dislocation multiplication. This results in a more effective strengthening response compared to the more widely spaced, larger precipitates formed during slow cooling. These findings emphasize that not only the precipitate volume fraction, but also the size and spatial distribution of precipitates must be carefully controlled to optimize mechanical properties.

4. Summary and conclusion

The precipitation and growth of γ′ during cooling after hot deformation and subsequent aging were investigated in VDM® Alloy 780 using in situ synchrotron HE-XRD. This study demonstrates the potential of HE-XRD to monitor microstructural evolution throughout a thermomechanical process chain. Complementary techniques (HV, TEM, and Thermo-Calc) supported the diffraction results.

Three different cooling rates (1000 °C/min, 100 °C/min, and 10 °C/min) resulted in the onset of γ′ precipitation at 811 °C, 918 °C, and 937 °C, respectively, with corresponding volume fractions of ~3 %, 14 %, and 20 %. The volume fraction evolution followed a sigmoidal trend for the tested cooling rates, indicating distinct stages of nucleation, growth, and coarsening. Slower cooling led to larger precipitate sizes.

Subsequent aging at 800 °C and 720 °C revealed a significant influence of the aging temperature on precipitation kinetics. At 800 °C, the equilibrium γ′ volume fraction was reached within 2.5 h, followed by coarsening, which stabilized after 4 h. In contrast, aging at 720 °C showed continuous increases in both volume fraction and precipitate size after 5 h, indicating that equilibrium was not yet reached. This is also reflected in the approximately 10 % lower HV10 values observed after aging at 720 °C compared to aging at 800 °C. These findings emphasize the strong impact of aging temperature and highlight how prior hot deformation promotes γ′ formation. They further underline the potential to tailor γ′ volume fraction and precipitate size through optimized aging strategies, thereby enabling precise adjustment of the alloy's mechanical performance for specific application requirements.

Table 4
Volume fraction and average precipitate size of VDM® Alloy 780 after hot deformation at 1000 °C cooling to RT with 1000 °C/min, aging at 800 °C and 720 °C, obtained by XRD, TEM, and TC.

Aging temperature [°C]	volume fraction [%]		precipitate size [nm]	
Technique	TC	XRD	XRD	TEM
800 °C	17.3	18.6 ± 0.1	18.8 ± 0.1	22.8 ± 6.3
720 °C	23.7	15.0 ± 0.1	9.1 ± 0.0	11.1 ± 2.6

Table 5
HV10 of the VDM® Alloy 780 samples after the aging heat treatment at 800 °C and 720 °C.

Aging temperature [°C]	HV10
800	446.4 (11.4)
720	404.5 (8.6)

CRediT authorship contribution statement

Massimo Fritton: Writing – original draft, Investigation, Formal analysis, Conceptualization. **Oliver Nagel:** Writing – review & editing, Investigation, Formal analysis. **Frank Kümmel:** Writing – review & editing, Investigation, Formal analysis. **Andreas Stark:** Investigation. **Masood Hafez-Haghighat:** Writing – review & editing, Resources, Investigation. **Bodo Gehrmann:** Resources, Investigation. **Steffen Neumeier:** Writing – review & editing, Supervision, Funding acquisition, Conceptualization. **Ralph Gilles:** Writing – review & editing, Supervision, Project administration, Funding acquisition.

Declaration of Competing Interest

The authors declare that they have no known competing financial interests or personal relationships that could have appeared to influence the work reported in this paper.

Acknowledgments

We gratefully acknowledge DESY (Hamburg, Germany), a member of the Helmholtz Association HGF, for providing the experimental facilities. This research was partially conducted at PETRA III, and we extend our thanks to Norbert Schell and Andreas Stark for their assistance with the HEMS beamline. We also appreciate the financial support from the BMBF Project "An innovative testing machine for heating, quenching, tension, compression and cracking studies of industrial relevant high-temperature alloys – HiMat (05K19WO7 and 05K19WEC).

Appendix A. Supporting information

Supplementary data associated with this article can be found in the online version at doi:10.1016/j.jallcom.2025.182111.

Data Availability

Data will be made available on request.

References

[1] M.C. Hardy, M. Detrois, E.T. McDevitt, C. Argyrakis, V. Saraf, P.D. Jablonski, J. A. Hawk, R.C. Buckingham, H.S. Kitaguchi, S. Tin, Solving recent challenges for wrought Ni-base superalloys, Metall. Mater. Trans. A 51 (6) (2020) 2626–2650.
[2] A.J. Goodfellow, E.I. Galindo-Nava, C. Schwalbe, H.J. Stone, The role of composition on the extent of individual strengthening mechanisms in polycrystalline Ni-based superalloys, Mater. Des. 173 (2019) 107760.
[3] J. Sharma, M.H. Haghighat, B. Gehrmann, C. Moussa, N. Bozzolo, Dynamic and Post-dynamic Recrystallization During Supersolvus Forging of the New Nickel-Based Superalloy—VDM Alloy 780, Superalloys 2020, Springer International Publishing, Cham, Switzerland, 2020, pp. 450–460.

[4] R. Cozar, A. Pineau, Morphology of γ′ and γ" precipitates and thermal stability of inconel 718 type alloys, MT 4 (1) (1973) 47–59.
[5] B. Hassan, J. Corney, Grain boundary precipitation in Inconel 718 and ATI 718Plus, Mater. Sci. Technol. 33 (16) (2017) 1879–1889.
[6] T. Fedorova, J. Rösler, J. Klöwer, B. Gehrmann, Development of a new 718-type Ni-Co superalloy family for high temperature applications at 750°C, MATEC Web Conf. 14 (2014) 01003.
[7] T. Fedorova, J. Rösler, B. Gehrmann, J. Klöwer, Invention of a New 718-Type Ni-Co superalloy family for high temperature applications at 750°C. 8th International Symposium on Superalloy 718 and Derivatives, John Wiley & Sons, Ltd, Chichester, England, UK, 2014, pp. 587–599.
[8] J. Rösler, T. Hentrich, B. Gehrmann, On the development concept for a new 718-type superalloy with improved temperature capability, Metals 9 (10) (2019) 1130.
[9] M. Fritton, F. Kümmel, A. Kirchmayer, A. Stark, M. Hafez Haghighat, B. Gehrmann, S. Neumeier, R. Gilles, Investigation of the hot deformation behavior in VDM® alloy 780 by in situ high-energy X-ray diffraction, Metall. Mater. Trans. A (2023) 1–15.
[10] C. Solís, J. Munke, M. Bergner, A. Kriele, M.J. Mühlbauer, D.V. Cheptiakov, B. Gehrmann, J. Rösler, R. Gilles, In situ characterization at elevated temperatures of a new Ni-based superalloy VDM-780 premium, Met. Mat. Trans. A 49 (9) (2018) 4373–4381.
[11] C. Solís, J. Munke, M. Hofmann, S. Mühlbauer, M. Bergner, B. Gehrmann, J. Rösler, R. Gilles, In situ characterization at high temperature of VDM Alloy 780 premium to determine solvus temperatures and phase transformations using neutron diffraction and small-angle neutron scattering, Miner. Met. Mater. Ser. (2019) 23–32.
[12] C. Ghica, C. Solís, J. Munke, A. Stark, B. Gehrmann, M. Bergner, J. Rösler, R. Gilles, HRTEM analysis of the high-temperature phases of the newly developed high-temperature Ni-base superalloy VDM 780 premium, J. Alloy. Compd. 814 (2020) 152–157.
[13] F. Kümmel, M. Fritton, C. Solís, A. Kriele, A. Stark, R. Gilles, Near-surface and bulk dissolution behavior of γ′ precipitates in Nickel-Based VDM® alloy 780 studied with in-situ lab-source and synchrotron X-ray diffraction, Metals 12 (7) (2022) 1067.
[14] D.A. Grose, G.S. Ansell, The influence of coherency strain on the elevated temperature tensile behavior of Ni-15Cr-AI-Ti-Mo alloys, Metall. Trans. A 12 (9) (1981) 1631–1645.
[15] M.V. Nathal, R.A. Mackay, R.G. Garlick, Temperature dependence of γ-γ' lattice mismatch in Nickel-base superalloys, Mater. Sci. Eng. 75 (1) (1985) 195–205.
[16] M.C. Hardy, M.H. Haghighat, C. Argyrakis, R.C. Buckingham, A. La Monaca, B. Gehrmann, The effect of microstructure on the strength of VDM Alloy 780. Proceedings of the 10th International Symposium on Superalloy 718 and Derivatives, Springer Nature Switzerland, Cham, Switzerland, 2023, pp. 29–47.
[17] M. Bergner, J. Rösler, B. Gehrmann, J. Klöwer, Effect of heat treatment on microstructure and mechanical properties of VDM alloy 780 premium, in: E. Ott, X. Liu, J. Andersson, Z. Bi, K. Bockenstedt, I. Dempster, J. Groh, K. Heck, P. Jablonski, M. Kaplan, D. Nagahama, C. Sudbrack (Eds.), Proceedings of the 9th International Symposium on Superalloy 718 & Derivatives: Energy, Aerospace, and Industrial Applications, Springer International Publishing, Cham, 2018, pp. 489–499.
[18] S.A. Sajjadi, H.R. Elahifar, H. Farhangi, Effects of cooling rate on the microstructure and mechanical properties of the Ni-base superalloy UDIMET 500, J. Alloy. Compd. 455 (1) (2008) 215–220.
[19] R. Gilles, D. Mukherji, H. Eckerlebe, L. Karge, P. Staron, P. Strunz, T. Lippmann, Investigations of early stage precipitation in a tungsten-rich nickel-base superalloy using SAXS and SANS, J. Alloy. Compd. 612 (2014) 90–97.
[20] C. Solís, A. Kirchmayer, I. da Silva, F. Kümmel, S. Mühlbauer, P. Beran, B. Gehrmann, M.H. Haghighat, S. Neumeier, R. Gilles, Monitoring the precipitation of the hardening phase in the new VDM® Alloy 780 by in-situ high-temperature small-angle neutron scattering, neutron diffraction and complementary microscopy techniques, J. Alloy. Compd. 928 (2022) 167203.
[21] M. Avrami, Kinetics of phase change. I general theory, J. Chem. Phys. 7 (12) (1939) 1103–1112.
[22] A.J. Ardell, The effect of volume fraction on particle coarsening: theoretical considerations, Acta Met. 20 (1) (1972) 61–71.
[23] P.W. Voorhees, The theory of Ostwald ripening, J. Stat. Phys. 38 (1) (1985) 231–252.
[24] P. Staron, T. Fischer, T. Lippmann, A. Stark, S. Daneshpour, D. Schnubel, E. Uhlmann, R. Gerstenberger, B. Camin, W. Reimers, E. Eidenberger, H. Clemens, N. Huber, A. Schreyer, In Situ experiments with synchrotron high-energy X-rays and neutrons, Adv. Eng. Mater. 13 (8) (2011) 658–663.
[25] A.P. Hammersley, FIT2D: a multi-purpose data reduction, analysis and visualization program, J. Appl. Crystallogr 49 (2) (2016) 646–652.
[26] J. Rodriguez-Carvajal, Fullprof A program for rietveld refinement and pattern matching analysis, in: Abstract of the Satellite Meeting on Powder Diffraction of the XV Congress of the IUCr, 1990, References - Scientific Research Publishing, Toulouse, France, 2022, p. 127.
[27] Industrial Applications of X-Ray Diffraction by Frank Smith (Z-lib.org), 2021.
[28] C.R.M. Afonso, G.T. Aleixo, A.J. Ramirez, R. Caram, Influence of cooling rate on microstructure of Ti–Nb alloy for orthopedic implants, Mater. Sci. Eng. C 27 (4) (2007) 908–913.
[29] A.J. Goodfellow, E.I. Galindo-Nava, K.A. Christofidou, N.G. Jones, T. Martin, P.A. J. Bagot, C.D. Boyer, M.C. Hardy, H.J. Stone, Gamma prime precipitate evolution during aging of a model nickel-based superalloy, Metall. Mater. Trans. A 49 (3) (2018) 718–728.
[30] M.A. Ali, I. López-Galilea, S. Gao, B. Ruttert, W. Amin, O. Shchyglo, A. Hartmaier, W. Theisen, I. Steinbach, Effect of γ′ precipitate size on hardness and creep properties of Ni-base single crystal superalloys: Experiment and simulation, Materialia 12 (2020) 100692.
[31] K. Maciejewski, H. Ghonem, Isotropic and kinematic hardening as functions of gamma prime precipitates in a nickel-based superalloy, Int. J. Fatigue 68 (2014) 123–135.
[32] W. Li, M. Vittorietti, G. Jongbloed, J. Sietsma, The combined influence of grain size distribution and dislocation density on hardness of interstitial free steel, J. Mater. Sci. Technol. 45 (2020) 35–43.
[33] K. Huang, K. Marthinsen, Q. Zhao, R.E. Logé, The double-edge effect of second-phase particles on the recrystallization behaviour and associated mechanical properties of metallic materials, Prog. Mater. Sci. 92 (2018) 284–359.
[34] H. Zhang, C. Li, Q. Guo, Z. Ma, Y. Huang, H. Li, Y. Liu, Hot tensile behavior of cold-rolled Inconel 718 alloy at 650 °C: the role of δ phase, Mater. Sci. Eng. A 722 (2018) 136–146.
[35] J. Ding, D. Neffati, Q. Li, R. Su, J. Li, S. Xue, Z. Shang, Y. Zhang, H. Wang, Y. Kulkarni, X. Zhang, Thick grain boundary induced strengthening in nanocrystalline Ni alloy, Nanoscale 11 (48) (2019) 23449–23458.
[36] M.D. Sangid, H. Sehitoglu, H.J. Maier, T. Niendorf, Grain boundary characterization and energetics of superalloys, Mater. Sci. Eng. A 527 (26) (2010) 7115–7125.
[37] E.O. Hall, The deformation and ageing of mild steel: III discussion of results, Proc. Phys. Soc. B 64 (9) (1951) 747.
[38] N.J. Petch, P. Stables, Delayed fracture of metals under static load - nature, Nature 169 (1952) 842–843.
[39] M. Hirata, K. Iwata, D. Okai, H. Adachi, Effect of precipitation size on dislocation density change during tensile deformation in Al–Zn–Mg alloy, Mater. Trans. 64 (11) (2023) 2584–2590.
[40] E.Y. Plotnikov, Z. Mao, S.-I. Baik, M. Yildirim, Y. Li, D. Cecchetti, R.D. Noebe, G. Martin, D.N. Seidman, A correlative four-dimensional study of phase-separation at the subnanoscale to nanoscale of a NiAl alloy, Acta Mater. 171 (2019) 306–333.
[41] C. Celada-Casero, J. Chao, E. Urones-Garrote, D. San Martin, Continuous hardening during isothermal aging at 723 K (450 °C) of a precipitation hardening stainless steel, Metall. Mater. Trans. A 47 (11) (2016) 5280–5287.
[42] W. Xia, X. Zhao, Q. Yue, L. Yue, J. Wang, Q. Ding, H. Bei, Z. Zhang, Formative and controlled mechanisms of nano-sized γ′ precipitates with local phase-transition within dislocation networks of nickel-based single crystal superalloys, Acta Mater. 206 (2021) 116653.